



# Canadian Geotechnical Journal

## Massive, continuous and non-invasive surface measurement of degree of saturation by shortwave infrared images

Journal:	<i>Canadian Geotechnical Journal</i>
Manuscript ID	cgj-2019-0051.R1
Manuscript Type:	Article
Date Submitted by the Author:	31-Oct-2019
Complete List of Authors:	Parera Morales, Ferran; Universitat Politècnica de Catalunya, Department of Civil and Environmental Engineering Pinyol, Núria; Centro Internacional de Metodos Numericos en Ingenieria, ; Universitat Politècnica de Catalunya, Civil and Environmental Engineering Alonso, Eduardo; Universitat Politècnica de Catalunya,
Keyword:	Degree of saturation, water content, infrared image, shortwave infrared (SWIR), laboratory tests
Is the invited manuscript for consideration in a Special Issue? :	Not applicable (regular submission)

SCHOLARONE™  
Manuscripts

1 Massive, continuous and non-invasive surface  
2 measurement of degree of saturation by  
3 shortwave infrared images  
4

5 Ferran Parera

PhD candidate

6 ferran.parera@upc.edu

7 Department of Civil and Environmental Engineering

8 Universitat Politècnica de Catalunya, Barcelona, Spain  
9

10 Núria M. Pinyol

Assitant Professor

11 nuria.pinyol@upc.edu

12 Two affiliations:

13 Department of Civil and Environmental Engineering

14 Universitat Politècnica de Catalunya, Barcelona, Spain  
15

16 Centre de Metodes Numerics en Enginyeria  
17

18 Eduardo E. Alonso

Professor of Geotechnical Engineering

19 eduardo.alonso@upc.edu

20 Department of Civil and Environmental Engineering

21 Universitat Politècnica de Catalunya, Barcelona, Spain  
22  
23

24 Corresponding author: Ferran Parera

25 Address: Campus Nord UPC. Building D2. 08034 Barcelona

26 Phone: 34 93 405 40 31

27 e-mail: ferran.parera@upc.edu  
28

## 29 ABSTRACT

30 Short wave infrared (SWIR) images provide an accurate procedure to measure the degree of  
31 saturation ( $S_r$ ) of soils. Changes in  $S_r$  result in reflectance changes which were recorded by a  
32 special digital camera optimized for a particular range of wavelengths which provide the  
33 maximum resolution of the method.

34 The paper describes the developed methodology, which relies on sample-determined  
35 calibration of soil reflectance for a few values of  $S_r$  covering the dry-fully saturated range of  
36 moistures.

37 The accuracy of the method was checked by comparing equilibrated profiles of SWIR-  
38 determined  $S_r$  with other procedures (sensor readings and water retention information).

39 It was found that the SWIR-based method correlates well with the degree of saturation of the  
40 soil but not with its water content, which may change, for a given  $S_r$ , when the soil deforms  
41 volumetrically.

42 The transient variations of  $S_r$  are also well captured by the method. The recorded evolution of  
43 two-dimensional  $S_r$  maps of an initially unsaturated soil column was satisfactorily compared  
44 with the results of a numerical model.

45

46 **Keywords:** Degree of saturation, water content, infrared image, shortwave infrared (SWIR),  
47 laboratory tests.

## 48 Introduction and fundamentals

49 In the experimental field of unsaturated soils, it is of interest to measure the degree of saturation  
50 ( $S_r$ ), water content, and suction because they control their mechanical and hydraulic behavior  
51 (Vanapalli and Mohamed 2007, Olivares et al. 2009, Chinkulkijniwat et al. 2016). The  
52 measurement of these inter-related variables is traditionally carried out by means of devices  
53 (tensiometers, hygrometers, capacitance sensors and dielectric sensors) that collect discrete

54 data in localized volumes. The placement of these sensors at or near the region of interest has  
55 to be selected a priori. However, the region of interest to measure such variables is, in some  
56 cases, unknown at the beginning of the test. This is, for instance, the case of scaled tests of slope  
57 failures in unsaturated soils in which the position of the failure surface, where the  $S_r$  value is of  
58 interest, cannot be specified at the beginning of the test.

59 As an alternative to sensors, other methods to evaluate the distribution of the degree of  
60 saturation or water content in soil have been explored. Neutron radiography and tomography  
61 were proposed as a non-invasive measurement of the water content (Tumlinson et al. 2008,  
62 Koliji et al. 2010, Cheng et al. 2012, Kim et al. 2012, Kang et al. 2014). These methods are based  
63 on the high neutron attenuation caused by the hydrogen of the water molecule compared to  
64 the interaction with the atoms of soil grains. This technique allows analyzing in 3D the entire  
65 sample, and it is useful to determine the hydraulic properties of granular soils. However, it  
66 presents some limitations for being used in general laboratory experiments. The technique is  
67 restricted to small samples that are placed in front of a neutron's beam. The procedure is based  
68 on the analysis of the neutrons that crosses the sample; therefore, the neutron penetration  
69 limits the thickness of the sample. The main difficulty is to manage the neutron radiation and  
70 induced radioactivity hazard, which implies the need to perform the experiments in isolated  
71 capsules or chambers.

72 On the other hand, two geophysical methods are useful to measure the  $S_r$  in soils. The electrical  
73 resistivity tomography is based on the different resistivity offered by soil particles and water to  
74 an electric current (Daily et al. 1992, Zhou et al. 2001). The ground-penetrating radar uses  
75 differences in the propagation velocity of electromagnetic microwaves (Greaves et al. 1996,  
76 Huisman et al. 2003). These two methods are well developed and useful for field measurements.  
77 They are capable of providing a 3D model for the soil  $S_r$ .

78 The aim of this study is to develop a method to be used in soil experiments in geotechnical  
79 laboratories. The outlined methods are not appropriate for this objective. Neutron radiography  
80 and other methods that use waves in the ultraviolet region of the electromagnetic spectrum are  
81 dangerous for biological tissues and they need to be performed in specialized laboratories. The  
82 ground-penetrating radar and other geophysical methods use long wavelengths. This length  
83 limits the maximum resolution physically attainable to centimetric pixel sizes. The sensors for  
84 long wavelengths are unable to get enough resolution for the laboratory tests of interest.

85 The suitable waves to measure the Sr are in the regions of the visual or infrared areas of the  
86 electromagnetic spectrum. Some authors have explored the possibilities of different ranges  
87 inside that area. The idea is to evaluate the amount of water filling the voids of soils taking  
88 advantage of the difference of light reflection/absorbance between water and solid particles.  
89 Water is more absorbent to light than solid soil particles, when analyzing the visible and infrared  
90 bands. Therefore, the amount of light reflected by a soil depends on its degree of saturation or,  
91 alternatively, on its water content. The soil appears darker the higher the amount of water. The  
92 physical principles of the light reflection in unsaturated soils are explained below.

93 Given a soil (characterized by mineral composition, grain size distribution, packing density, grain  
94 surface roughness), the presence of the water surrounding the soil grains causes a change in  
95 scattering and absorption of the incident light. A comprehensive explanation of the effect of  
96 water on the light reflectance was given by Nolet et al. (2014) after briefly describing the  
97 theoretical background. Under dry conditions, the reflectance is controlled by the soil  
98 mineralogy and structure. When some water is added to the soil (Figure 1a), water is held in the  
99 soil as adsorbed water films around the solid grains. At this condition, the optical path length in  
100 the water is close to zero, and the decrease of spectral reflectance is almost solely due to  
101 scattering. As the water content increases (Figure 1b), water meniscus form bridges between  
102 grains, which increase the optical path length, resulting in an increase of absorption. When the

103 soil becomes fully saturated (Figure 1c) and the free water appears at the surface being  
104 evaluated, the optical path length in water is at its maximum, and the reflectance of the soil is  
105 mainly defined by the water coefficient of light absorption (Hillel 1998, Lobell and Asner 2002).

106 The most sensitive bands of the electromagnetic spectrum to assess the amount of water in the  
107 soil are a result of the physical principles governing the interaction between light and water. The  
108 quantum theory explains that the absorption of light by matter is determined by stable quantum  
109 changes in its atomic and molecular energies. The bands of the electromagnetic spectrum whose  
110 energy coincide with stable quantum changes would tend to be absorbed.

111 In the specific case of the water molecule, the wavelength bands, on the visible and infrared  
112 area of the electromagnetic spectrum that coincide with stable quantum changes, correspond  
113 to changes in the vibrational state of the water molecule ( $\nu$ ). The water molecule has three  
114 vibration modes: symmetric stretch ( $\nu_1$ ), bending deformation ( $\nu_2$ ), and asymmetric stretch ( $\nu_3$ ).  
115 Stable vibration excited states correspond to specific combinations of these three modes of  
116 vibration. The wavelengths whose energy coincides with one of these stable excited vibration  
117 states tend to be absorbed and retained by the water molecule. (Table 1).

118 Lobell and Asner (2002), Knadel et al. (2014), Nolet et al. (2014), Sadeghi et al. (2015), Tian and  
119 Philpot (2015) carried out specific tests, using laboratory spectroscopy, to analyse the effect of  
120 moisture on the reflectance of different soils for different wavelengths of light spectrum. Leu  
121 (1977) and Shuchman and Rea (1981) evaluated other soil properties affecting the reflectance.

122 Figure 2 plots the results of one of the mentioned laboratory spectroscopy tests as an example  
123 (Nolet et al. 2014). The reflectance of sand at different  $S_r$  values was measured in the laboratory  
124 by means of a full range spectrometer (300-2500 nm). For a given wavelength, the reflectance  
125 decreased with increasing amount of water. The magnitude of this variation depends on the  
126 wavelength. Figure 2 highlights the bands of light absorbance by water, defined in Table 1  
127 (Wozniak and Dera 2006). The comparison between the two superimposed plots indicates that

128 the wavelengths where the soil reflectance is more affected by moisture variations coincide with  
129 the bands with higher coefficient of light absorption by water. With the aim of correlating the  
130 reflectance with moisture, it is convenient to select the wavelength ranges most sensitive to  
131 water content. On the visual and infrared areas, the two most convenient wavelength ranges  
132 are 1400 -1550 nm and 1900 – 2000 nm. Notice that the most absorbent bands lay on the Short-  
133 Wave InfraRed (SWIR) part of the electromagnetic spectrum, whereas in the visible part the  
134 absorbance is almost negligible.

135 The effect of changing soil saturation on the light reflectance has been evaluated in the literature  
136 for different soils (from coarse sand to silty loam). This information is collected in Figure 3. In all  
137 cases, the maximum difference between the reflectance for dry and saturated conditions is  
138 reached in the range of 1400 -1550 nm and 1900 – 2000 nm. This observed response is mainly  
139 controlled by the optical properties of the water, which exhibits an absorption peak for these  
140 two wavelength ranges.

141 Soranzo et al. (2015) evaluated the degree of saturation in natural soils by means of the analysis  
142 of visual images (wavelengths: 400-800 nm). For the range of wavelengths of the visual  
143 spectrum, the effect of the  $S_r$  on the reflectance is not enough to provide a proper precision in  
144 the correlation between reflectance and  $S_r$ . To overcome this limitation, Peters et al. (2011),  
145 Siemens et al. (2013, 2014) and Sills et al. (2017) use artificial transparent soils with the same  
146 reflection than the fluid used and a black background. By measuring the light reflected at the  
147 air-fluid contacts, they are able to estimate the amount of air in the sample and, therefore, to  
148 calculate the degree of saturation.

149 Sadeghi et al. (2015) based on previous theories, proposed a linear physically-based model to  
150 transform the light reflectance from images at different wavelengths to the soil water content.  
151 The technique is especially useful in satellite imaging. Later on, Sadeghi et al. (2017) applied the  
152 method for the characterization and quantification of liquid distribution in porous media from

153 SWIR images. Their model enables to convert the SWIR reflectance into soil water content. The  
154 proposed methodology was successfully validated for soils with different grain size distributions.

155 This paper presents a methodology to determine the continuous variation of  $S_r$  in unsaturated  
156 porous media by interpreting SWIR images. The procedure can be applied to surface images. It  
157 relies on a calibrated set of correlations between light reflectance and the measured  $S_r$  of  
158 samples of the soil being tested. This correlation was found to be nonlinear unlike previous  
159 results by Sadeghi et al. (2015).

160 At the medium scale of a laboratory experiment (an equilibrated column of unsaturated sand  
161 above a zero suction level), the SWIR-based method was consistent with other direct (sensors)  
162 and indirect (through the water retention relationship) procedures to find the saturation profile.

163 The ultimate goal of the research presented was to build case records at laboratory mid-scale  
164 (1g and eventually ng) to validate the hydro-mechanical behaviour of unsaturated soils under  
165 changing boundary conditions. In this regard, there was an interest in determining the moisture-  
166 related index, either water content or degree of saturation, offering the best correlation with  
167 SWIR images. The results of tests on samples at different void ratios but constant water content  
168 will be given.

169 In a final part of the paper, the experimental transient variation of  $S_r$  of an unsaturated soil  
170 column, subjected to surface infiltration, is compared with the results of a calculation by means  
171 of the finite element code CODE-BRIGHT (Olivella et al., 1996, 2019).

## 172 Experiment description

173 The purpose of the test performed is to measure the  $S_r$  of unsaturated soil surfaces by  
174 correlating the light reflectance with the  $S_r$ . The procedure requires previous calibration carried  
175 out on samples with a known  $S_r$ . Based on the spectrometry studies discussed above, the



176 wavelength used in this work is 1500-1560 nm. This specific range was selected because of the  
177 capabilities of the camera selected.

### 178 *Camera*

179 Images of unsaturated samples are captured by a Short-Wave InfraRed (SWIR) camera. Common  
180 SWIR cameras use the InGaAs sensor. This is a specialized and expensive technology. As an  
181 alternative, the common sensor used in digital cameras (CCD array charge-coupled device) can  
182 be used after a phosphor-coated treatment (which is significantly cheaper). In the experiments  
183 presented in this paper, the CamIR sensor from Scintacor is used. The camera should not have  
184 any gain or automatic image improvement to avoid additional pixel intensity changes not caused  
185 by the soil reflectivity. The sensor (Sony progressive scan interface interline transfer ICX445 1/3"  
186 Exview HAD CCDTM), after the phosphor treatment, has two spectral sensitivity peaks at 1512  
187 and 1540 nm (Figure 4).

188 Energy-efficient infrared lightbulbs of 175W are used as a light source. Other options that could  
189 be used are incandescent tungsten light bulbs (dismissed due to the low energy-efficiency) or  
190 Sunlight (dismissed due to the lack of intensity control). Normal LED or CFL lights cannot be used  
191 as a light source because they emit only in the visible spectrum.

192 The illumination must be constant throughout the experiment because the light reflected  
193 depends on the reflectivity index but also on the amount of incident light. Therefore, all the  
194 experiments of a set shall be performed with the same lightbulb arrangement and camera  
195 distance.

### 196 *Material*

197 The soil used in the test is calcareous-siliceous fine sand from Castelldefels' beach (Catalonia,  
198 Spain). The properties are summarized in Table 2. The soil-water retention curve (SWRC), under  
199 imbibition conditions, was measured by the gravimetric method in a segmented hanging

200 column. The measured values of  $S_r$  and suction are indicated in Figure 5 together with the  
201 estimated Van Genuchten model (van Genuchten 1980). Table 2 shows the values of the model  
202 parameters.

### 203 *Measuring the reflectance*

204 The method requires the measurement of the reflectance in granular materials. The pixel  
205 intensity, which is a measure of the reflectance, is also known as grey value in the photography  
206 filed. It ranges from 0 (black color) to 255 (white color).

207 Consider a homogeneous and unsaturated sample (150x250 mm) of Castelldefels' sand whose  
208 bottom is saturated, and the  $S_r$  reduces with height in a situation of equilibrium. Figure 6 shows  
209 digital images of this sample taken at visible light spectrum (Figure 6a) and at an infrared  
210 wavelength (SWIR) (Figure 6b). The varying  $S_r$  results in a gradual color variation from the light  
211 color of the upper part of the sample to the darker color of the saturated bottom.

212 Due to the texture of the soil, the different colors of the sand grains, and the phosphor-coated  
213 treatment to transform the visual sensor into a SWIR sensor, the image exhibits "salt-and-  
214 pepper" noise. This noise implies that the discrete information from each single pixel (in this  
215 case 1x1 mm) does not represent the general reflection of the surrounding area, which depends  
216 on the  $S_r$ . Therefore, an analysis based on pixel intensity cannot be correlated with the  $S_r$ , and  
217 a pixel intensity of a representative area for each pixel is required.

218 In order to wane the salt-and-pepper noise, the intensity of each pixel is calculated as a weighted  
219 average of the intensity of the pixels located in the vicinity of a given location by means of a  
220 Gaussian filter. The average pixel intensity value ( $\xi_{x_0, y_0}$ ) associated with a pixel located at  
221 coordinates  $(x_0, y_0)$  is computed by means of the 2-dimensional Gaussian function centered on  
222 the pixel evaluated:

$$\xi_{x_0 y_0} = \sum \xi_{xy} \frac{1}{2\pi\sigma^2} e^{-\frac{(x-x_0)^2+(y-y_0)^2}{2\sigma^2}} \quad \text{Equation 1}$$

223 where  $\xi_{xy}$  is the pixel intensity of a pixel located at coordinates  $(x,y)$ , and  $\sigma$  is the standard  
 224 deviation of the Gaussian function. The suitable value of the standard deviation mainly depends  
 225 on: the noise from the camera sensor, the grain size and the expected spatial gradient of the Sr.  
 226 Figure 7 shows the SWIR image of the sample after applying the Gaussian filter with a standard  
 227 deviation of 20 pixels. Each point of the filtered image stores the information of the surrounding  
 228 pixels, weighted by the distance following a Gaussian normal distribution. As a reference, for  
 229 the indicated standard deviation, weights are 68.27%, 27.18% and 4.28% at distances of 20, 40  
 230 and 60 pixels respectively.

## 231 Calibration

232 The calibration procedure allows correlating the SWIR reflectance of soil samples with the Sr  
 233 value. SWIR images of a set of samples of Castelldefels' sand having the same density and  
 234 different water contents were analyzed. The calibration will provide a curve correlating the pixel  
 235 intensity with the Sr.

236 The samples were prepared in cylindrical containers, 7.1 cm of diameter and 3.6 cm high (Figure  
 237 8). The camera and two infrared lightbulbs were fixed in position. Zenithal images were taken  
 238 with the SWIR camera. All the samples were placed under the fixed camera in the same place in  
 239 order to maintain a constant intensity of incident light.

240 Eight samples compacted at  $1390 \text{ kg/m}^3$  of dry density and different degrees of saturation (0,  
 241 0.02, 0.07, 0.15, 0.30, 0.44, 0.60, 0.73 and 1) were evaluated. The hygroscopic moisture of the  
 242 dry sample was assumed to be negligible, and its Sr is indicated as 0. A maximum Sr of 1 was  
 243 also tested. Sr values over 0.7 are difficult to obtain because the air tends to get trapped

244 between the soil grains. Degrees of saturation close to one were reached by pluviating soil  
 245 particles into water, following a procedure proposed by Ezzein and Bathurst (2011).

246 Table 3 shows the SWIR images of the samples after applying the Gaussian filter (applying a  
 247 standard deviation of 50 pixels) and the values of water content,  $S_r$  and pixel intensity.

248 Figure 9, based on Table 3, shows the curves correlating the  $S_r$  and the pixel intensity. The  
 249 correlation curve of Figure 9 depends not only on the type of soil, density and  $S_r$ , but also on the  
 250 intensity of the incident light. It follows that this curve cannot be used to evaluate the  $S_r$  of  
 251 samples of the same soil from SWIR images taken under different light intensity because the  
 252 light intensity changes the absolute value of the reflectance. However, for a given light intensity,  
 253 the measured pixel intensity values can be normalized taking into account the extreme cases:  
 254 dry ( $S_r = 0$ ) and fully saturated ( $S_r = 1$ ). The following normalized pixel intensity is defined:

$$\xi_{norm} = \frac{\xi - \xi_{dry}}{\xi_{sat} - \xi_{dry}} \quad \text{Equation 2}$$

255 where  $\xi_{sat}$  and  $\xi_{dry}$  is the pixel intensity at saturated and dry conditions, respectively. Then  
 256 the correlation  $S_r$  vs normalized pixel intensity ( $\xi_{norm}$ ) becomes independent of the light  
 257 intensity. Figure 10 shows the normalized calibration curve for the samples analyzed. The curve  
 258 was smoothly extrapolated close to the saturation.

259 Sadeghi et al. (2015) propose another type of model based on the physical equation of  
 260 reflectance and absorbance that does not require a calibration curve for each soil. This model is  
 261 useful when the soil cannot be tested, such as remote sensing using satellite images.

262 *Effect of void ratio*

263 An additional set of calibration experiments was performed to evaluate the effect of the  
264 variation of void ratio on the SWIR reflectance. The variation of this state parameter was key to  
265 discern if reflectance was controlled by the soil degree of saturation or by water content.

266 Three samples of sand were prepared assigning a certain value of water content to each one of  
267 them. The sand was placed in a metallic cylinder, and the top was covered by a glass. The bottom  
268 base of the cylinder had a piston to change the volume of the sample. In this way, the void ratio  
269 could be controlled. Reducing the void ratio, the  $S_r$  increases maintaining constant the water  
270 content (Table 5). A SWIR image was taken for each of the cases presented in Table 5. Table 6  
271 shows the average pixel intensity measured on each sample surface.

272 If the water content controls the reflectance, the pixel intensity should be constant regardless  
273 of the void ratio changes. Otherwise, if the  $S_r$  controls the reflectance, the pixel intensity should  
274 decrease with higher void ratios. The results are plotted in Figure 11 and Figure 12, which show  
275 the correlation between the pixel intensity with the  $S_r$  and the water content, respectively. In  
276 Figure 11 the pixel intensity decreases as the  $S_r$  increases following approximately the  
277 calibration curve determined in the previous section. It follows that the reflection is not  
278 controlled exclusively by the water content but the void ratio has a significant role. This is further  
279 illustrated in Figure 12: the samples have different pixel intensity values at the same water  
280 content, but varying the void ratio. These figures show that the reflectance/absorbance is  
281 determined by  $S_r$ , which is the variable assessed with SWIR images.

282 Figure 13 summarizes the normalized pixel intensity –  $S_r$  curves for all the samples tested. The  
283  $S_r$  of the samples indicated was imposed by different procedures. The constant dry density (1390  
284  $\text{kg/m}^3$ ) curve plotted (orange) was determined for the calibration procedure (Figure 10). The  
285 variation of  $S_r$  was imposed by increasing the water content. The second curve (blue), at a higher  
286 dry density (1470  $\text{kg/m}^3$ ), was determined following the same procedure. In the three additional

287 curves (yellow, lime, green) shown in the plot discussed in the previous paragraphs (Figure 11),  
288 the variation of  $S_r$  was imposed by increasing the density (in the range 1290 – 1560 kg/m<sup>3</sup>) at  
289 constant water content. There is some scatter in the plot, but it is clear that the  $S_r$  is the  
290 dominant parameter explaining the soil reflectance for the tested densities.

## 291 Analysis

292 Once the calibration is achieved, this section presents the steps to assess the  $S_r$  based on SWIR  
293 images. The method can be applied to a sequence of images in order to evaluate not only the  
294 distribution of the  $S_r$  at a certain time, but also its variation in time. The steps are described  
295 below and indicated in the flowchart of Figure 14 for a SWIR video recording. The analysis will  
296 be carried out for each extracted frame from the video images.

### 297 *Steps*

- 298 1. Record the laboratory experiment with the SWIR camera, and extract the frames from the  
299 video.
- 300 2. Each image is stored as a matrix where each position corresponds to the *pixel intensity* of  
301 every pixel.
- 302 3. The Gaussian filter is applied
- 303 4. *The Point of Interest (POI)* coordinates are selected or imported.
- 304 5. The area of interest is selected or imported.
- 305 6. The *pixel intensity matrix* ( $\xi$ ) is created storing the pixel intensity of the points of interest that  
306 are inside the area of interest.
- 307 7. The *normalized pixel intensity matrix* ( $\xi_{norm}$ ) is created, normalizing the values of the *pixel*  
308 *intensity matrix* ( $\xi$ ).
- 309 8a. The  $S_r$  and the *water content* of every point of interest is calculated from the *normalized*  
310 *pixel intensity matrix* ( $\xi_{norm}$ ) using the calibration curves.

311 8b. The calibration curves come from the calibration process performed once for each material.  
312 The curves provide the relationship between the *normalized pixel intensity* of the calibration  
313 images and their *Sr* or *water content*.  
314 9. *Suction* is calculated from the *Sr* using the Water Retention Curve of the material.  
315 10. The results can be plotted on contour graphs providing the spatial distribution of the variable  
316 of interest (*Sr*, *water content*, *suction*) at any time *t* (Figure 19). The histories of desirable  
317 variables may be built at any point of interest (Figure 20).

## 318 Validation and evaluation

319 The proposed method is applied in this section to measure the distribution of the *Sr* in a column  
320 of an unsaturated Castelldefels' sandy soil using the calibration curve of Figure 10. The  
321 experiment is divided into two stages: (a) stationary stage after imposing the saturation of the  
322 bottom of the column; and (b) transient stage during a wetting process from the top of the  
323 column. In order to validate the method, the measurements of the *Sr* based on SWIR images  
324 are compared with measurements taken by means of conventional moisture sensors installed  
325 in the sample at different elevations.

### 326 *Experimental setup*

327 The experiment was performed on a column of sand placed in a perspex transparent tank except  
328 for the frontal side that was made of glass to avoid scratches that could affect the quality of the  
329 images. The tank was 400 mm high, 1000 mm long (limited to 200mm by adding a glass wall)  
330 and 200 mm deep. The sand sample tested was a column with square cross-sectional area,  
331 200x200mm, and a height of 300 mm (Figure 15). The tank base was filled with a 2 cm thick layer  
332 of gravel which was covered with a geotextile to avoid sand penetration into the gravel layer.  
333 The top was covered by a plastic film to minimize evaporation without affecting the atmospheric  
334 pressure. The sand was placed in the tank by dry pluviation and the density was controlled by

335 weighting sequentially the amount of soil. The average density of the sample is  $1500 \text{ kg/m}^3$ .  
336 Three capacitive soil moisture sensors (SEN0193) were installed at different heights: 60, 140 and  
337 220 mm.

338 Two wetting situations (stages) were analyzed:

339 **First stage:** The bottom of the sample is saturated imposing a stable water level at the top of  
340 the gravel layer located at the bottom of the sample. The water rose up through the sand by  
341 capillarity until it reached the stationary condition. At this time, the lateral surface of the column  
342 was recorded by means of the SWIR camera and the  $S_r$  was estimated by analyzing the image.

343 **Second stage.** The soil column is wetted from the top with a water flow applied, simulating  
344 rainfall, using a drip system with nozzles separated 10 mm. The vertical water infiltration process  
345 in time was recorded using the SWIR camera. The time evolution of the distribution of the  $S_r$  on  
346 the sample face will be analyzed.

## 347 *Results*

### 348 *First stage*

349 Once the condition of saturation was fixed on the bottom of the sandy column, the water rose  
350 up progressively through the sand. Equilibrated and stable conditions were reached two weeks  
351 after the saturation of the base.

352 Figure 16 shows the distribution of the  $S_r$  and water content at the stationary condition  
353 measured by means of the SWIR image, following the procedure presented before and the  
354 calibration curves of Figure 9.

355 Several vertical profiles of the SWIR-measured  $S_r$  are plotted in Figure 17. They are compared  
356 with the theoretical vertical profile computed by accepting a linear increase of the suction with  
357 height, applying the previously determined retention curve (approximated by the Van



358 Genuchten expression, Figure 5). In addition, the values of the  $S_r$  measured by moisture sensors  
359 are also indicated. The average dry density ( $1500 \text{ kg/m}^3$ ) was used to compute the water content  
360 from  $S_r$  measurements.

361 The results using the calibration curve method and the linear physically-based method (Sadeghi  
362 et al. 2015) are plotted in Figure 18. The comparison shows that while the linear method exhibits  
363 a satisfactory performance, the results using the calibration curve method fit better the  
364 expected water retention curve and the direct measurements with sensors. The proposed  
365 method needs the calibration of a specific curve for each soil that is possible inside the facilities  
366 of a geotechnical lab, but not in other cases where the linear method would be more useful.

#### 367 *Second stage*

368 The rainfall applied to the second stage of the experiment had an intensity of  $0.6425 \text{ mm/s}$   
369 (equivalent to a flow rate of  $0.0257 \text{ l/s}$  on a  $200 \times 200 \text{ mm}$  area). The infiltration process was  
370 recorded with a SWIR camera at 15 frames per second. However, one image per second is  
371 enough for the presented application. The time evolution of the SWIR-estimated  $S_r$  is plotted in  
372 Figure 19.

373 The measured values by means SWIR images and the values measured by moisture sensors are  
374 compared in Figure 20. The evolution of the  $S_r$  at three heights, by means of SWIR images, match  
375 well the direct measurements by moisture sensors. The evolution of the descending waterfront  
376 is also well captured by the image analysis.

#### 377 **Numerical model**

378

379 The experiment has been modelled using the finite element program Code\_Bright (Olivella et  
380 al. 1996; 2019). The model only used hydraulic equations for the solution. The water retention  
381 curve used in the numerical simulation was the Van Genuchten model (Equations 3 and 4):

$$S_e = \frac{S_l - S_{rl}}{S_{ls} - S_{rl}} = \left( 1 + \left( \frac{P_g - P_l}{P} \right)^{\frac{1}{1-\lambda}} \right)^{-\lambda} \quad \text{Equation 3}$$

$$P = P_0 \frac{\sigma}{\sigma_0} \quad \text{Equation 4}$$

382 The hydraulic properties of the sand introduced as model parameters are described in Table 4.

383 The numerical water retention curve is compared with the experimental curve measured in the  
384 laboratory in Figure 21.

385 The liquid phase relative permeability follows Equation 5.

$$k_{rl} = S_e^5 \quad \text{Equation 5}$$

386 It is represented in Figure 22. The permeability rises as it gets closer to the saturated level to  
387 take into account the reduction of pore volume due to the soil collapse caused by saturation.

388 The time evolution of the SWIR-measured  $S_r$  is compared to the results from the Code\_Bright  
389 numerical simulation.

390 The measured values by means SWIR images are compared to the values measured by moisture  
391 sensors and to the values calculated by the numerical simulation (Figure 23). The evolution of  
392 the  $S_r$  at three heights, by means of SWIR images, match the direct measurements by moisture  
393 sensors.

394 Figure 24 shows the spatial distribution of the  $S_r$  in certain times and compares the  
395 measurements by SWIR images and the results from the numerical simulation. The descent of  
396 the waterfront follows the same general evolution. Nevertheless, the measurements on the  
397 images show the inhomogeneities on the distribution of the  $S_r$ . In the real experiment, the  
398 effects of spatial variation of hydraulic properties result in preferential paths for water flow and

399 an irregular waterfront which are features not captured by the numerical simulation because  
400 there was no attempt to introduce any heterogeneity in the model. The opportunity to measure  
401 and map the spatial distribution of the Sr allows a better understanding the real behaviour of  
402 the soil during the whole experiment and provides a benchmark for a refined analysis

## 403 Discussion

404 The results shown in this work were obtained for a fine sand. Correlation between pixel intensity  
405 and water content has also been validated for other grain size distribution with satisfactory  
406 results (Sadeghi et al., 2017). The procedure presented should be evaluated and validated in  
407 different kind of soils in order to define the range of applicability of the method regarding the  
408 type of soils and in particular, the applicability in clays.

409 The methodology presented exhibits the following limitations:

410 **Non-uniform incident light:** The method is based on the light reflected by the soil, but the  
411 reflection is dependent on the intensity of the incident light. In order to keep the incident light  
412 intensity stable through time, the arrangement of the light emitters can be fixed if the  
413 experiments are performed in the same location. In spite of having a stable light intensity  
414 through time, the intensity cannot be spatially homogeneous because the light comes from  
415 point sources (Figure 25). The intensity of light that reaches the experiment surface depends on  
416 the distance to the emitter. These factors force to normalize the calibration and the pixel  
417 intensity values from the images.

418 In order to get better control of the incident light is also useful to include distributed targets  
419 with known reflectance values in the image. These targets would act as a reference points to  
420 normalize the pixel intensity values, instead of using the saturated and dry pixel intensity.

421 **Image edges:** The images from the camera should be filtered, as discussed above (using a  
422 Gaussian filter) to attenuate the effect of the different grain mineralogy and the sensor noise.

423 This filter makes the pixel intensity from the background interfere in the filtered values close to  
424 the edges. This effect should be taken into account when interpreting the results near the edge.  
425 The  $S_r$  values close to the boundaries may appear higher than they really are.

426 **Surface measurements:** The penetration of the SWIR electromagnetic waves into the soil is low.  
427 Therefore, the technique is only capable of assessing the  $S_r$  of the surface of the soil samples  
428 tested.

## 429 Conclusions

430 This study presents a method to measure the degree of saturation of unsaturated soil in  
431 laboratory experiments by means of the optical sensing of soil reflectance using short wave  
432 infrared (SWIR) images. The method accuracy relies on the differential spectral absorbance of  
433 water partially filling the soil pores and the solid grains. Among the analyzed range of light  
434 wavelengths, the SWIR spectrum is the most absorbent.

435 An affordable SWIR camera alternative to the most expensive InGaAs sensor cameras is  
436 proposed. The performance of the camera is judged to be sufficient for the purposes of  
437 determining of the soil's  $S_r$ . The testing arrangement of the camera and the light sources must  
438 be stable for a proper analysis.

439 SWIR images interpreted by a filtered and normalized pixel intensity was shown to depend on  
440 the  $S_r$  (and not on water content). An initial experimental calibration, for a given soil, is required  
441 to relate pixel intensity and  $S_r$ . A benchmark experiment conducted on an unsaturated soil  
442 column in equilibrium with a saturated lower boundary (suction increases linearly with elevation  
443 above the base) allowed to compare the derived water retention curve with a direct  
444 determination by standard procedures. The agreement was very satisfactory (Figure 17).

445 In a second benchmark experiment, during a surface wetting (simulating rainfall) of the previous  
446 column, SWIR results were compared with the readings of moisture sensors located in the  
447 column. Again, the correspondence was very good (Figure 20).

448 These benchmarks indicate that the method may be as accurate as other known procedures  
449 based on “point” sensors. However, the main value of the method is its capability to capture  
450 two-dimensional fields of evolving Sr. This is a major advantage to design experiments to  
451 validate numerical models in boundary value problems.

## References

- 452 Cheng, C.L., Kang, M., Perfect, E., Voisin, S., Horita, J., Bilheux, H.Z., Warren, J.M., Jacobson, D.L.,  
453 and Hussey, D.S. 2012. Average Soil Water Retention Curves Measured by Neutron  
454 Radiography. *Soil Science Society of America Journal*, **76**(4): 1184. The Soil Science Society  
455 of America, Inc. doi:10.2136/sssaj2011.0313.
- 456 Chinkulkijniwat, A., Yubonchit, S., Horpibulsuk, S., Jothityangkoon, C., Jeptaku, C., and  
457 Arulrajah, A. 2016. Hydrological responses and stability analysis of shallow slopes with  
458 cohesionless soil subjected to continuous rainfall. *Canadian Geotechnical Journal*, **53**(12):  
459 2001–2013. NRC Research Press. doi:10.1139/cgj-2016-0143.
- 460 Daily, W., Ramirez, A., LaBrecque, D., & Nitao, J. 1992. Electrical resistivity tomography of vadose  
461 water movement. *Water Resources Research*, **28**(5), 1429-1442.
- 462 Ezzein, Fawzy M., and Richard J. Bathurst. 2011 A transparent sand for geotechnical laboratory  
463 modeling. *Geotechnical Testing Journal* **34.6** : 590-601.
- 464 van Genuchten, M.T. 1980. A Closed-form Equation for Predicting the Hydraulic Conductivity of  
465 Unsaturated Soils1. *Soil Science Society of America Journal*, **44**(5): 892.  
466 doi:10.2136/sssaj1980.03615995004400050002x.
- 467 Greaves, R. J., Lesmes, D. P., Lee, J. M., & Toksöz, M. N. 1996. Velocity variations and water  
468 content estimated from multi-offset, ground-penetrating radar. *Geophysics*, **61**(3), 683-  
469 695.
- 470 Hillel, D. 1998. *Environmental soil physics*. Elsevier, San Diego, CA.
- 471 Huisman, J. A., Hubbard, S. S., Redman, J. D., & Annan, A. P. 2003. Measuring soil water content

- 472 with ground penetrating radar. *Vadose zone journal*, 2(4), 476-491.
- 473 Kang, M., Perfect, E., Cheng, C.L., Bilheux, H.Z., Lee, J., Horita, J., and Warren, J.M. 2014. Multiple  
474 pixel-scale soil water retention curves quantified by neutron radiography. *Advances in*  
475 *Water Resources*, **65**: 1–8. Elsevier. doi:10.1016/J.ADVWATRES.2013.12.004.
- 476 Kim, F.H., Penumadu, D., and Hussey, D.S. 2012. Water Distribution Variation in Partially  
477 Saturated Granular Materials Using Neutron Imaging. *Journal of Geotechnical and*  
478 *Geoenvironmental Engineering*, **138**(2): 147–154. doi:10.1061/(ASCE)GT.1943-  
479 5606.0000583.
- 480 Knadel, M., Deng, F., Alinejadian, A., Wollesen de Jonge, L., Moldrup, P., and Greve, M.H. 2014.  
481 The Effects of Moisture Conditions—From Wet to Hyper dry—On Visible Near-Infrared  
482 Spectra of Danish Reference Soils. *Soil Science Society of America Journal*, **78**(2): 422. The  
483 Soil Science Society of America, Inc. doi:10.2136/sssaj2012.0401.
- 484 Koliji, A., Vulliet, L., and Laloui, L. 2010. Structural characterization of unsaturated aggregated  
485 soil. *Canadian Geotechnical Journal*, **47**(3): 297–311. doi:10.1139/T09-089.
- 486 Leu, D.J. 1977. Visible and near — infrared reflectance of beach sands: A study on the spectral  
487 reflectance/ grain size relationship. *Remote Sensing of Environment*, **6**(3): 169–182.  
488 Elsevier. doi:10.1016/0034-4257(77)90002-5.
- 489 Lobell, D.B., and Asner, G.P. 2002. Moisture Effects on Soil Reflectance. *Soil Science Society of*  
490 *America Journal*, **66**(3): 722–727.
- 491 Nolet, C., Poortinga, A., Roosjen, P., Bartholomeus, H., and Ruessink, G. 2014. Measuring and  
492 Modeling the Effect of Surface Moisture on the Spectral Reflectance of Coastal Beach Sand.  
493 *PLoS ONE*, **9**(11): 1–9. doi:10.1371/journal.pone.0112151.
- 494 Olivares, L., Damiano, E., Greco, R., Zeni, L., Picarelli, L., Minardo, A., Guida, A., and Bernini, R.  
495 2009. An Instrumented Flume to Investigate the Mechanics of Rainfall-Induced Landslides  
496 in Unsaturated Granular Soils. *Geotechnical Testing Journal*, **32**(2): 101366. ASTM  
497 International. doi:10.1520/gtj101366.
- 498 Olivella, S., Gens, A., Carrera, J., and Alonso, E.E. 1996. Numerical formulation for a simulator  
499 (CODE\_BRIGHT) for the coupled analysis of saline media. *Engineering Computations*, **13**(7):  
500 87–112. MCB UP Ltd. doi:10.1108/02644409610151575.
- 501 Olivella, S., Vaunat, J., Rodríguez-Dono, A. (2019) Code\_Bright User's Guide. Version 9.  
502 [https://deca.upc.edu/en/projects/code\\_bright](https://deca.upc.edu/en/projects/code_bright)

- 503 Peters, S.B., Siemens, G., and Take, W.A. 2011. Characterization of Transparent Soil for  
504 Unsaturated Applications. *Geotechnical Testing Journal*, **34**(5): 103580. ASTM  
505 International. doi:10.1520/GTJ103580.
- 506 Sadeghi, M., Jones, S.B., and Philpot, W.D. 2015. A linear physically-based model for remote  
507 sensing of soil moisture using short wave infrared bands. *Remote Sensing of Environment*,  
508 **164**: 66–76. Elsevier. doi:10.1016/J.RSE.2015.04.007.
- 509 Sadeghi, M., Sheng, W., Babaeian, E., Tuller, M., and Jones, S.B. 2017. High-Resolution  
510 Shortwave Infrared Imaging of Water Infiltration into Dry Soil. *Vadose Zone Journal*, **16**(13):  
511 0. The Soil Science Society of America, Inc. doi:10.2136/vzj2017.09.0167.
- 512 Shuchman, R.A., and Rea, D.K. 1981. Determination of beach sand parameters using remotely  
513 sensed aircraft reflectance data. *Remote Sensing of Environment*, **11**: 295–310. Elsevier.  
514 doi:10.1016/0034-4257(81)90027-4.
- 515 Siemens, G.A., Peters, S.B., and Take, W.A. 2013. Comparison of confined and unconfined  
516 infiltration in transparent porous media. **49**(February 2012): 851–863.  
517 doi:10.1002/wrcr.20101.
- 518 Siemens, G.A., Take, W.A., and Peters, S.B. 2014. Physical and numerical modeling of infiltration  
519 including consideration of the pore-air phase 1. **1487**(October): 1475–1487.
- 520 Sills, L.-A.K., Mumford, K.G., and Siemens, G.A. 2017. Quantification of Fluid Saturations in  
521 Transparent Porous Media. *Vadose Zone Journal*, **16**(2): 0. GeoScienceWorld.  
522 doi:10.2136/vzj2016.06.0052.
- 523 Soranzo, E., Tamagnini, R., and Wu, W. 2015. Face stability of shallow tunnels in partially  
524 saturated soil: centrifuge testing and numerical analysis. *Géotechnique*, **65**(6): 454–467.  
525 Thomas Telford Ltd. doi:10.1680/geot.14.P.123.
- 526 Tian, J., and Philpot, W.D. 2015. Relationship between surface soil water content, evaporation  
527 rate, and water absorption band depths in SWIR reflectance spectra. *Remote Sensing of*  
528 *Environment*, **169**: 280–289. Elsevier. doi:10.1016/J.RSE.2015.08.007.
- 529 Tumlinson, L.G., Liu, H., Silk, W.K., and Hopmans, J.W. 2008. Thermal Neutron Computed  
530 Tomography of Soil Water and Plant Roots. *Soil Science Society of America Journal*, **72**(5):  
531 1234. Soil Science Society. doi:10.2136/sssaj2007.0302.
- 532 Vanapalli, S.K., and Mohamed, F.M.O. 2007. Bearing Capacity of Model Footings in Unsaturated  
533 Soils. *In* *Experimental Unsaturated Soil Mechanics*. Springer Berlin Heidelberg, Berlin,

- 534 Heidelberg. pp. 483–493. doi:10.1007/3-540-69873-6\_48.
- 535 Wozniak, B., and Dera, J. 2006. Light Absorption in Sea Water. Springer New York, New York, NY.  
536 doi:10.1007/978-0-387-49560-6.
- 537 Zhou, Q. Y., Shimada, J., & Sato, A. 2001. Three-dimensional spatial and temporal monitoring of  
538 soil water content using electrical resistivity tomography. Water Resources Research,  
539 37(2), 273-285.
- 540

Draft



Table 1. Bands of the electromagnetic spectrum with high absorbance coefficient by water, beside the correspondent vibrational state of the excited water molecule (Wozniak and Dera 2006).



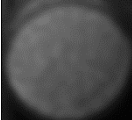




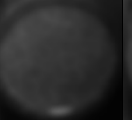
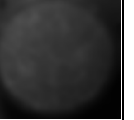
Symbol	Wavelength	Assignment
$\alpha$	739 nm	$av_1 + bv_3; a + b = 4$
$\mu$	836 nm	$av_1 + v_2 + bv_3; a + b = 3$
$\rho \sigma \tau$	970 nm	$av_1 + bv_3; a + b = 3$
$\phi$	1200 nm	$av_1 + v_2 + bv_3; a + b = 2$
$\psi$	1470 nm	$av_1 + bv_3; a + b = 2$
$\Omega$	1900 nm	$av_1 + v_2 + bv_3; a + b = 1$

Draft

Table 2. Geotechnical properties of Castelldefels' sand.

Parameter	Units	Value
Particle density	g/cm <sup>3</sup>	2.665
Dry density	g/cm <sup>3</sup>	min – max
Porosity		1.442 – 1.795
Particle size distribution		0.459 – 0.326
D10	mm	0.254
D30	mm	0.3109
D60	mm	0.3715
Air-entry value	kPa	0.7
Van Genuchten parameters: $S_r = S_{r_r} + \frac{(S_{r_s} - S_{r_r})}{[1 + (\alpha h)^n]^m}$		
$\alpha$		0.07
$n$		2.2
$m$		0.545
$S_{r_s}$		0.73
$S_{r_r}$		0
Saturated permeability at a porosity of 0.4	m/s	$2 \cdot 10^{-4}$

Table 3. SWIR images after Gaussian filter and parameters of the sample used in the calibration.

<b>Water content</b>	0	0.73	2.63	5.26	10.53	15.79	21.05	26.35	30.00
<b>Sr</b>	0	0.02	0.07	0.15	0.30	0.44	0.60	0.73	1
									
<b>Pixel intensity</b>	104	92	86	83	78	71	64	54	52

Draft

Table 4. Hydraulic properties of the sand.

<b>Parameter</b>	<b>Symbol</b>	<b>Units</b>	<b>Value</b>
Pore pressure	$P_0$	MPa	0.0012
Surface tension	$\sigma_0$	N/m	0.072
Shape function	$\lambda$		0.8
Residual saturation	$S_{r1}$		0
Maximum saturation	$S_{1s}$		1
Intrinsic permeability	$K_0$	$m^2$	4e-11

Draft

Table 5. Degree of saturation of tested samples. For each water content, three different degrees of saturation are obtained by reducing the void ratio.

		Void ratio		
		0.70	0.82	1.08
Water content	7.1	0.28	0.24	0.18
	14.3	0.56	0.48	0.36
	22.9	0.90	0.77	0.58

Draft

Table 6. Average pixel intensity of each sample condition presented in Table 5.

		Void ratio		
		0.70	0.82	1.08
Water content	7.14	171	174	177
	14.29	130	133	159
	22.86	106	109	139

Draft

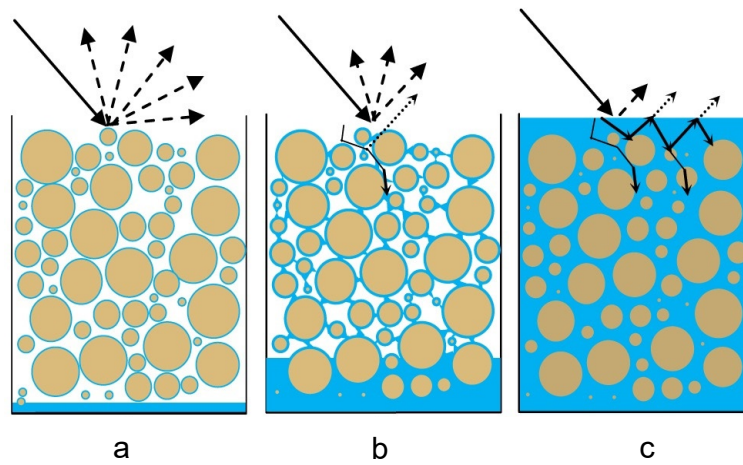


Figure 1. Schematic representation of the effect of water content on light absorbance and reflectance of a sandy soil sample surface. Changes in degree of saturation lead to different water distribution into the soils: (a) Water films around the sand grains; (b) Capillary menisci between grains; (c) Saturation and continuous water (Nolet et al. 2014).

Draft

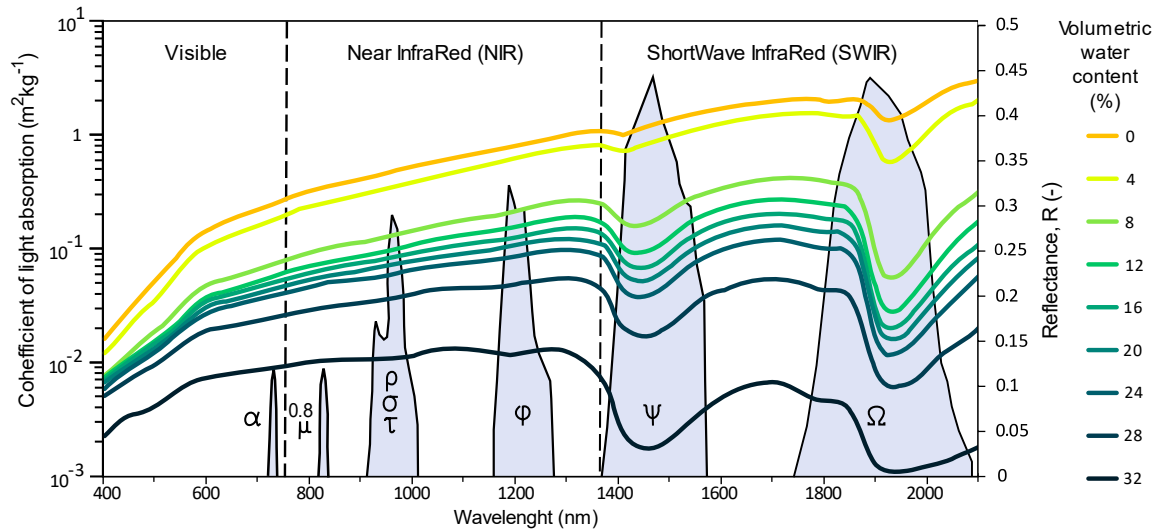


Figure 2. Curves indicating the measured spectral reflectance of a beach sand over a range of 350-2100 nm in samples with different values of degree of saturation (Nolet et al. 2014). The underlaid grey zone indicates the coefficient of light absorption by water depending on the wavelength according to Table 1 (Wozniak and Dera 2006).

Draft



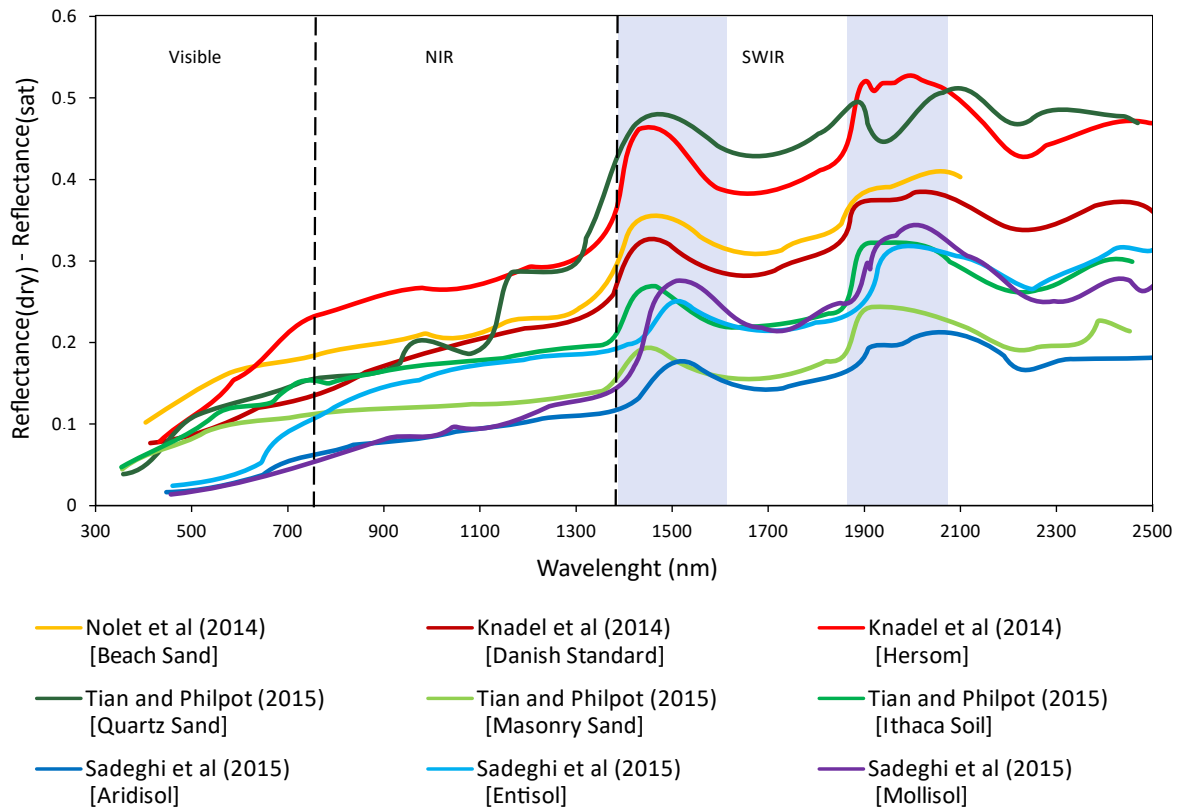


Figure 3. Variation, for different soils, of the difference between the reflectance measured at dry and saturated conditions for varying wavelengths of different soils. Shaded areas (1400 -1550 nm and 1900 – 2000 nm) corresponds to maximum differences.

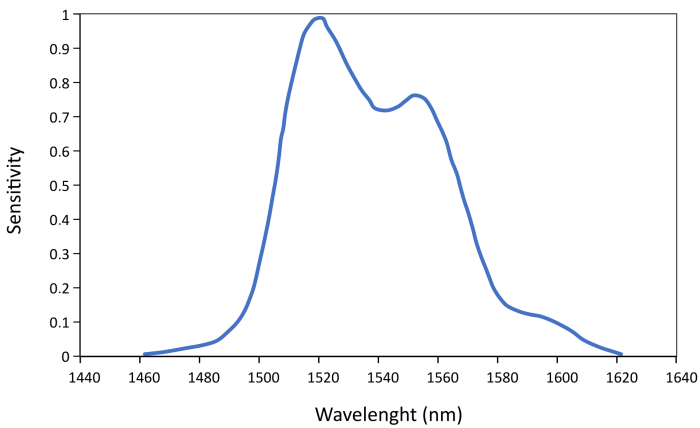


Figure 4. Sensitivity curve of the camera phosphor treated sensor.

Draft

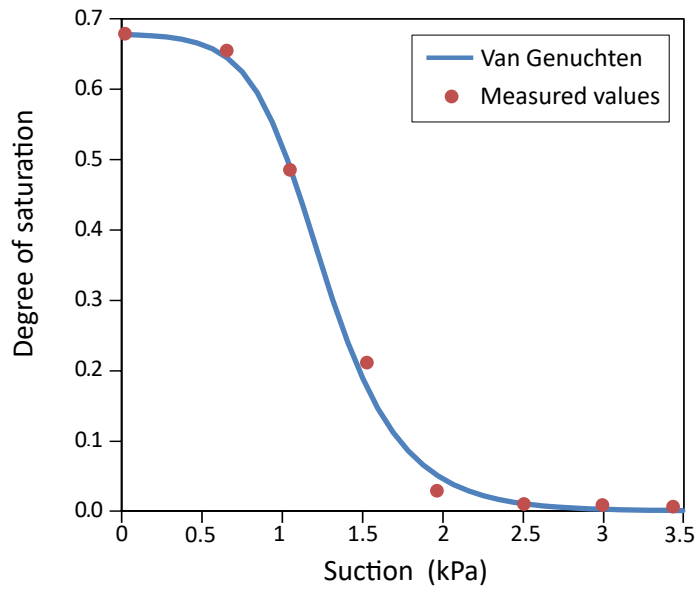


Figure 5 Measured values and calibrated water retention curve of Castelldefels' beach sand.

Draft

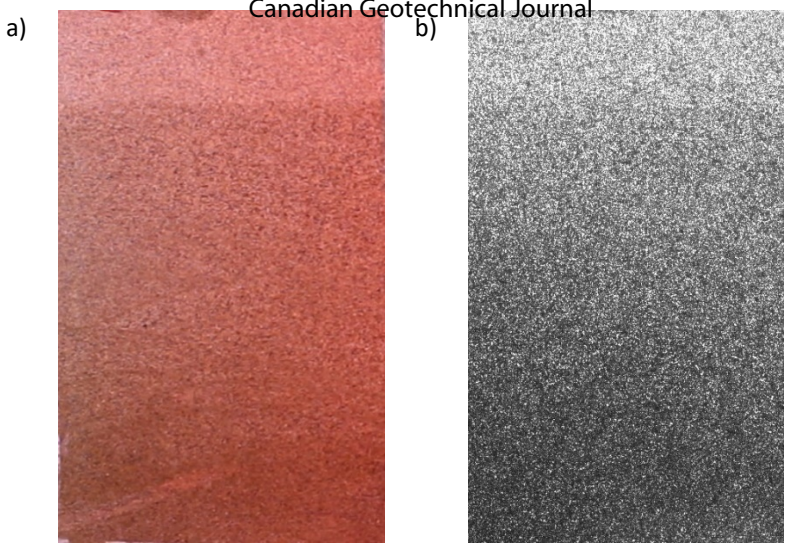


Figure 6 Images of an unsaturated column of Castelldevens beach sand in (a) the visible and (b) the SWIR spectra.

Draft

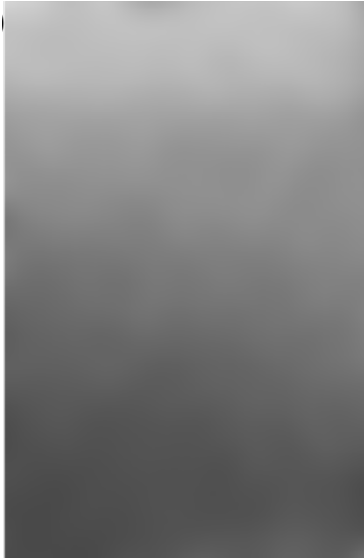


Figure 7 SWIR image after a Gaussian filter.

Draft

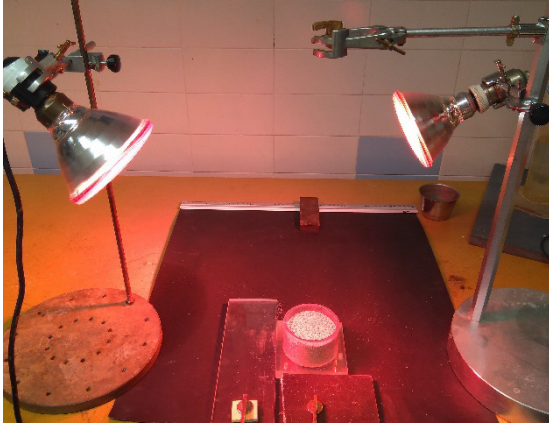


Figure 8 Experiment setup for calibration.

Draft

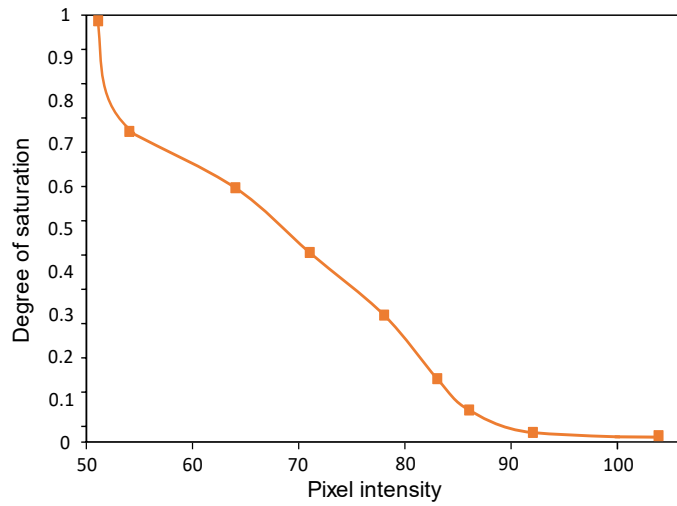


Figure 9 Correlation curve between the degree of saturation and pixel intensity measured in samples.

Draft

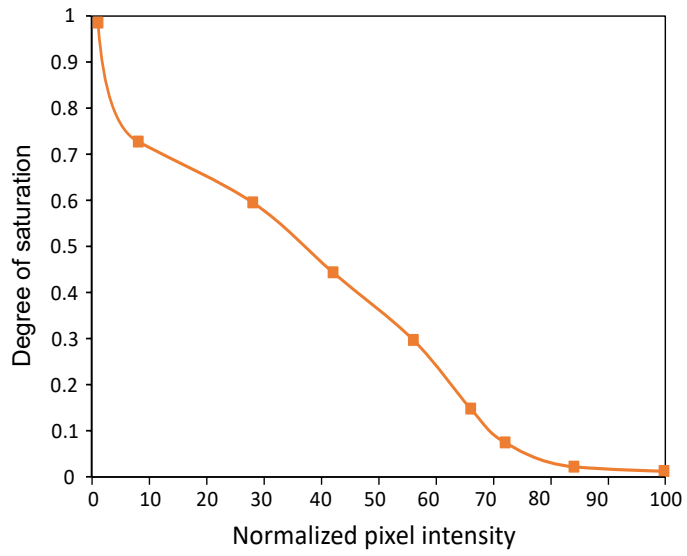


Figure 10 Calibration curve correlating normalized pixel intensity and degree of saturation measured in samples.

Draft



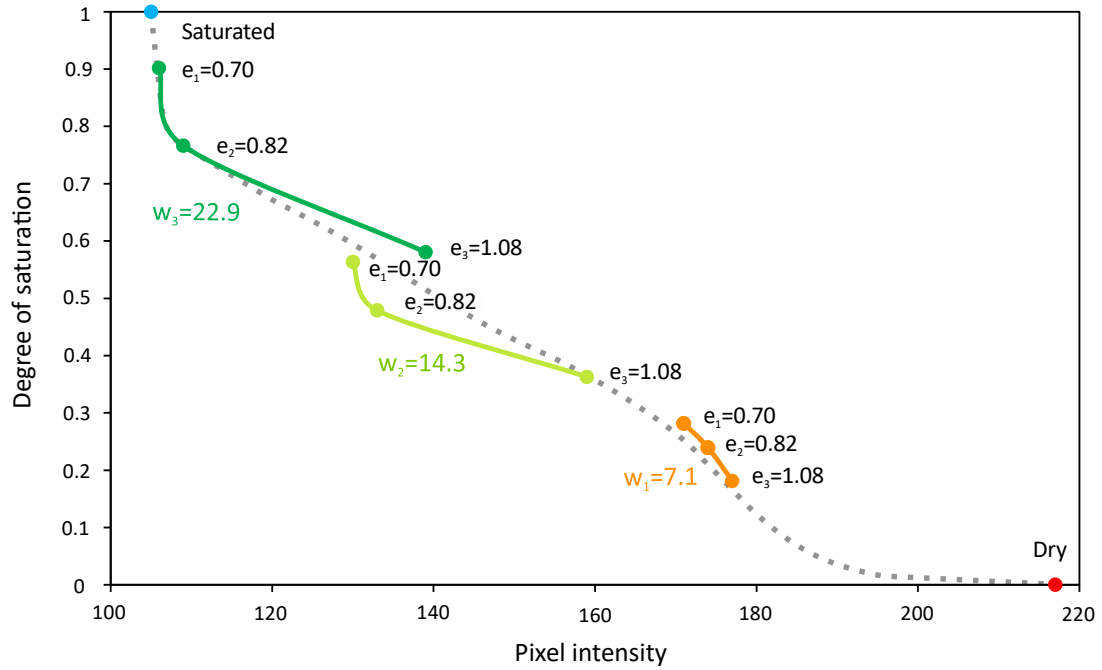


Figure 11 Effect of the void ratio on the reflectance of the soil for the different water contents (7.14, 14.29, 22.86). The pixel intensity for dry and saturated conditions is also plotted as a reference. The average trend is plotted as a dotted line.

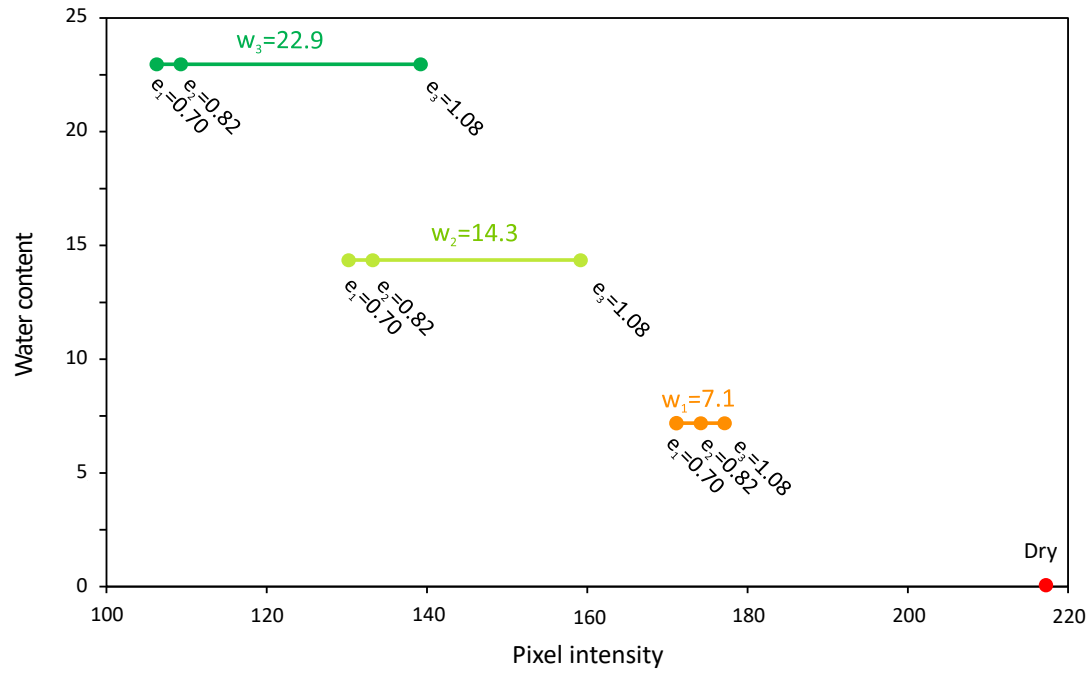


Figure 12 Pixel intensity variation of samples having the same water content but different void ratio.

Draft

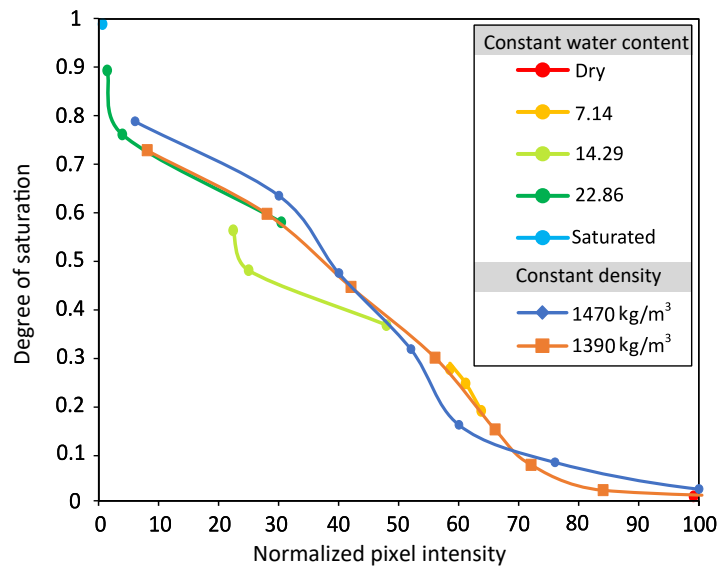


Figure 13 Normalized pixel intensity – Degree of saturation plot of soil samples at constant water content (7.14, 14.29, 22.86) and varying void ratio. Normalized pixel intensity – degree of saturation plot of samples at constant density (1470, 1390 kg/m<sup>3</sup>) and varying water content.

Draft

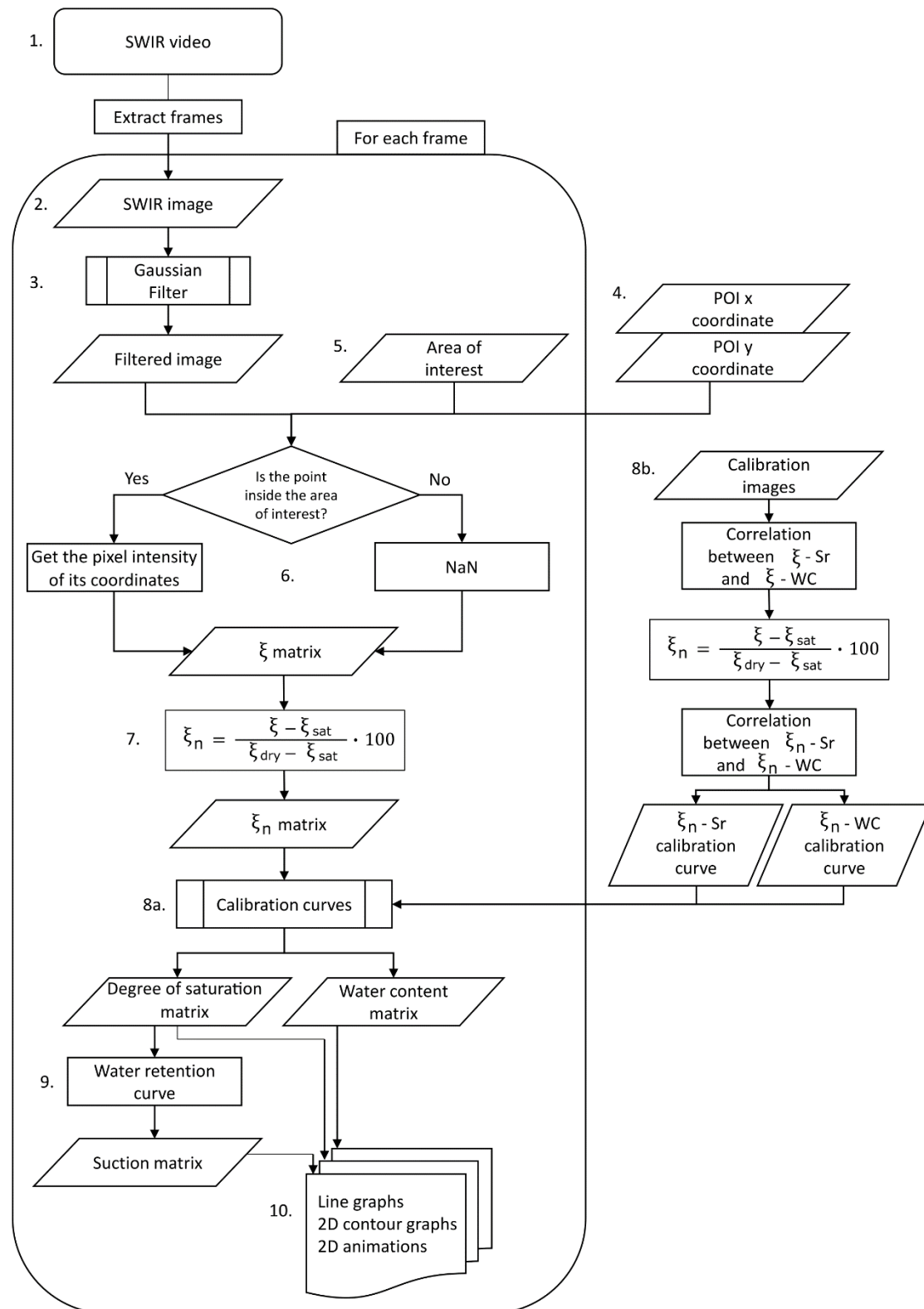


Figure 14 Flowchart of the methodology.

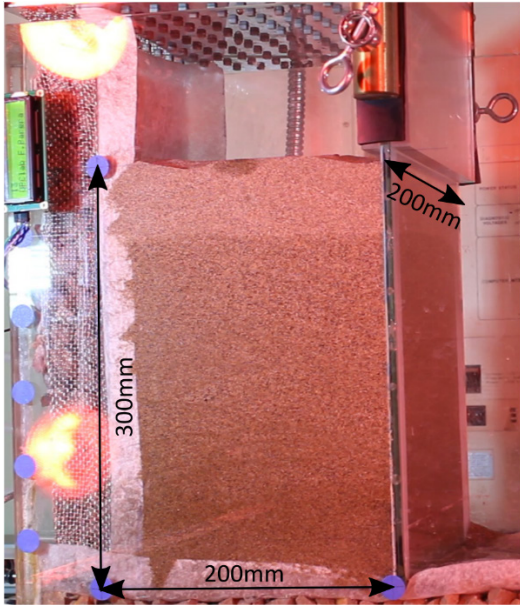


Figure 15 Experiment setup for validation

Draft

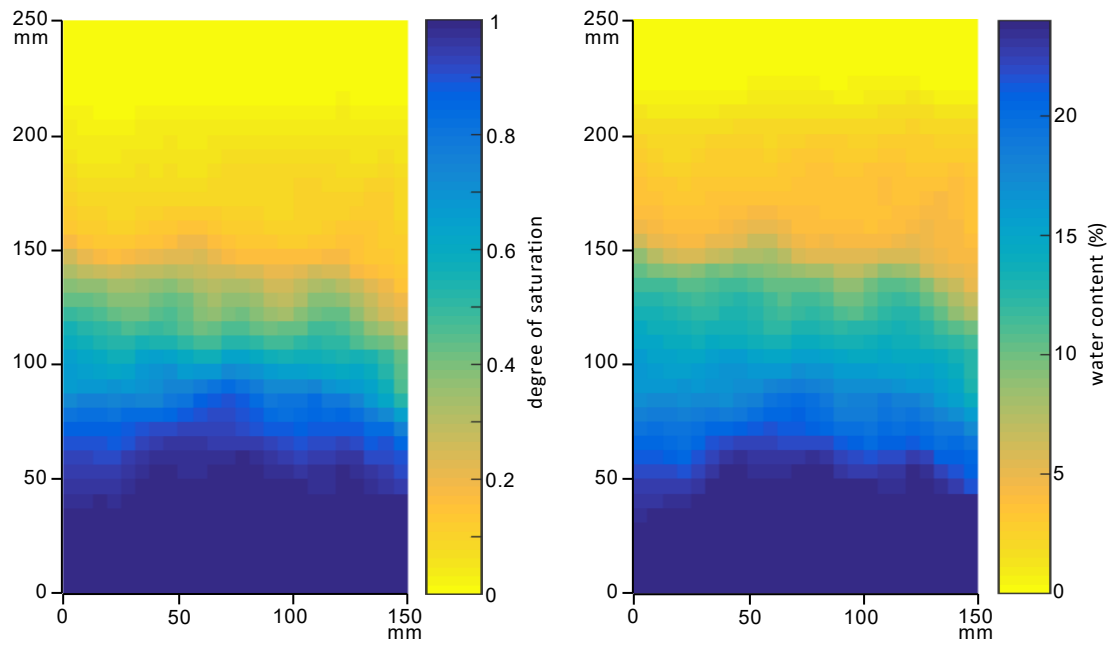


Figure 16 Values of (a) degree of saturation and (b) water content of the column measured by the SWIR image.

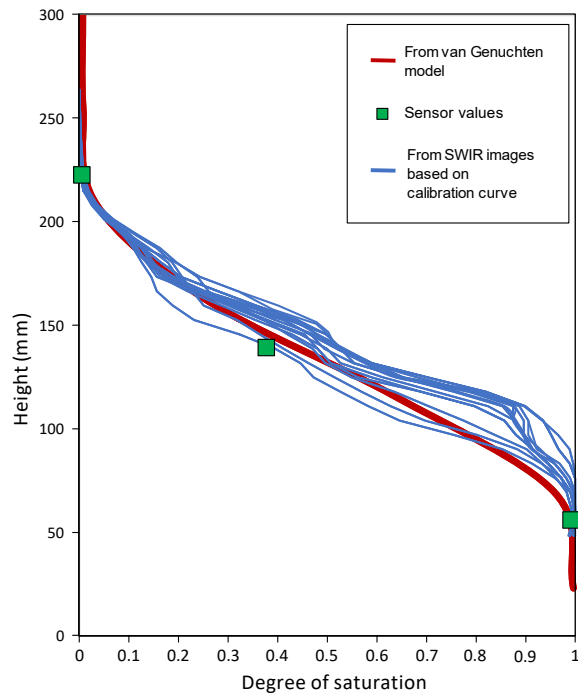


Figure 17 Comparison of vertical profiles of degree of saturation determined by SWIR images and values computed from equilibrium suction profile and the experimental water retention curve.

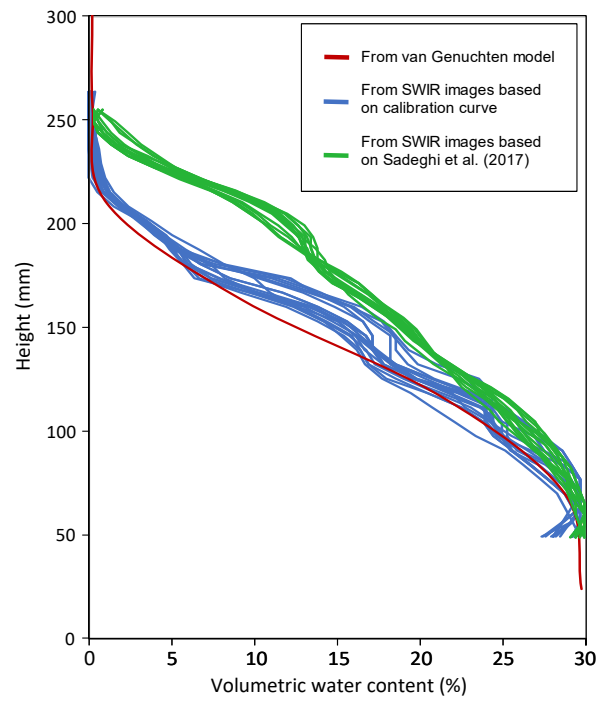


Figure 18 Comparison of vertical profiles of volumetric water content assessed by SWIR images compared experimental water retention curve. a) Using a calibration curve developed for this soil. b) Using the linear physical-based method (Sadeghi et al. 2015, 2017).

Draft



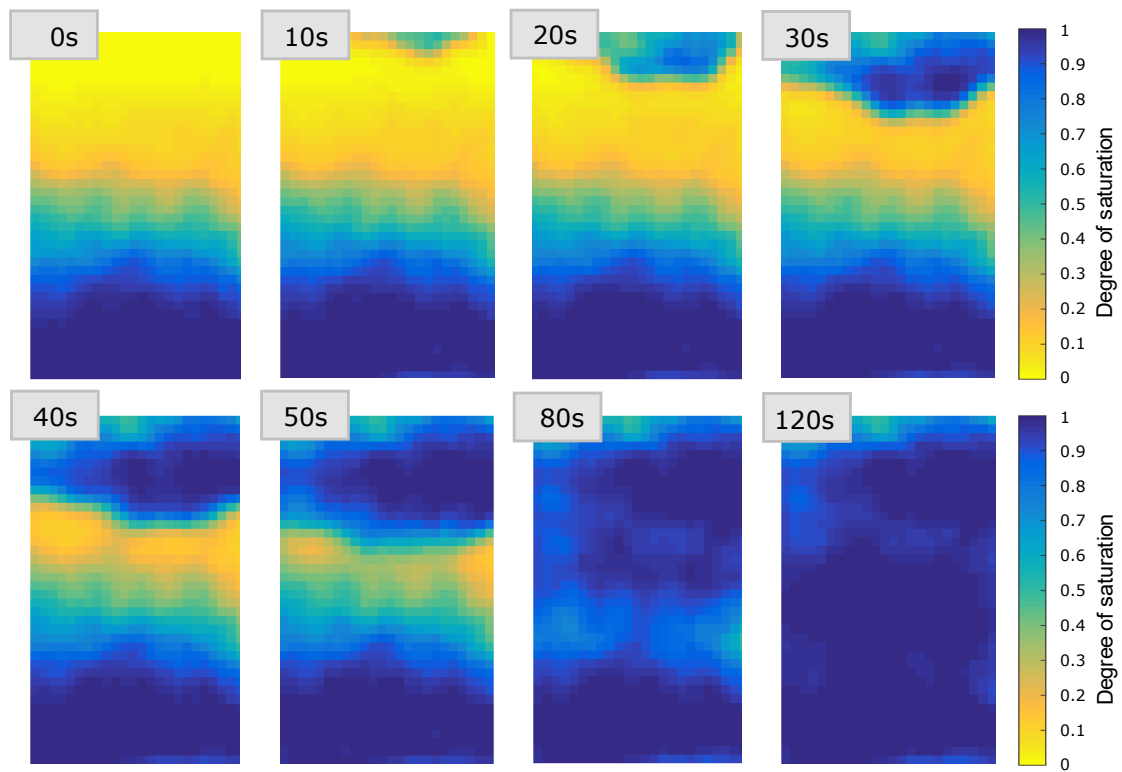


Figure 19 SWIR-measured degree of saturation at increasing time during the raining sequence.

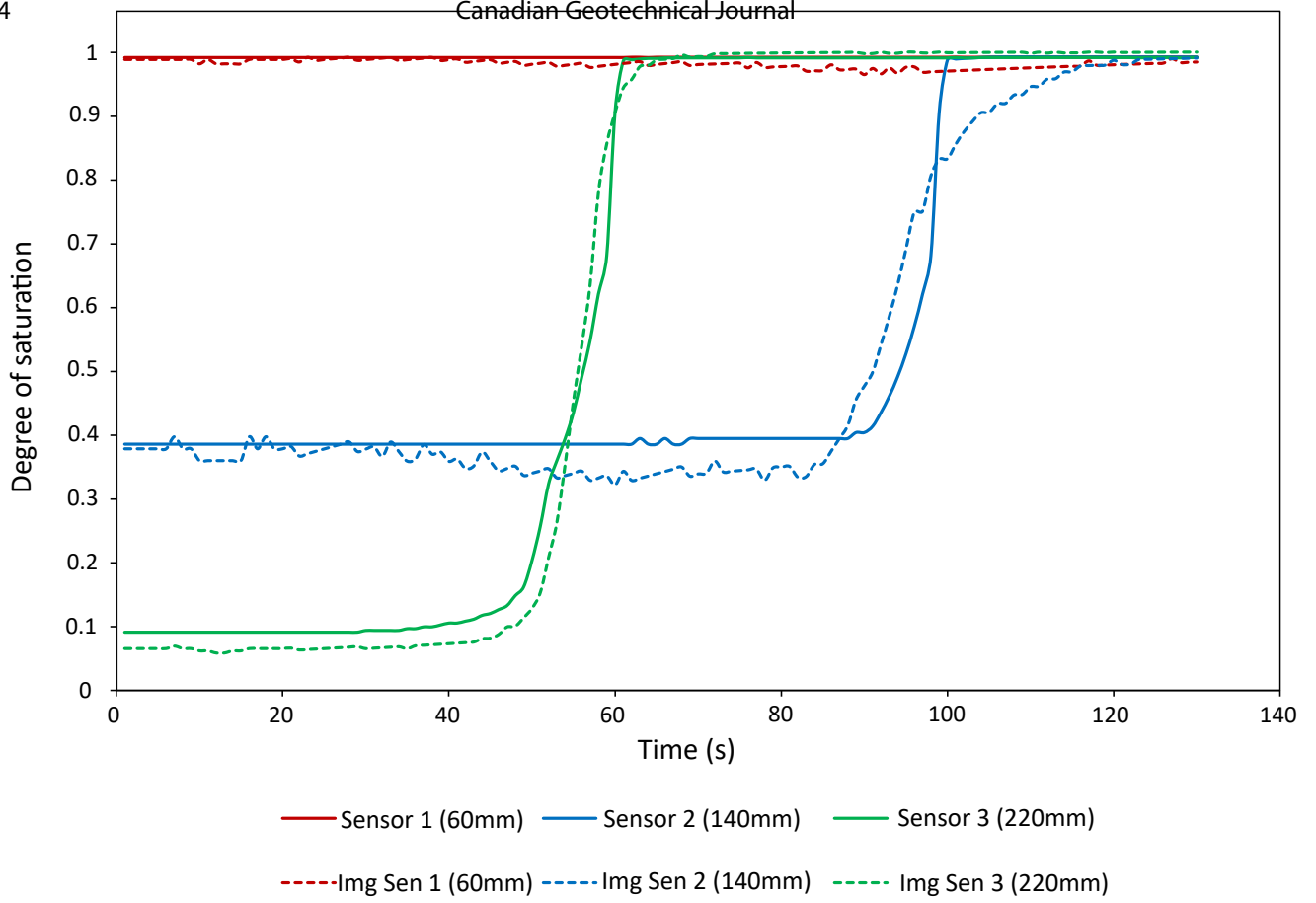


Figure 20 Comparison between the degree of saturation measured by SWIR images (dashed line) and by moisture sensors at three column heights (60 mm, 14 mm and 220 mm)

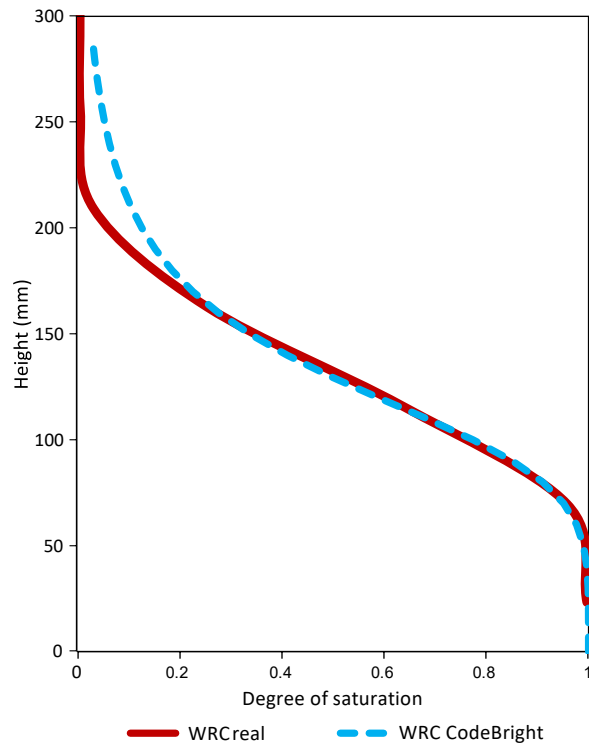


Figure 21 Comparison between the experimental and the numerical water retention curve.

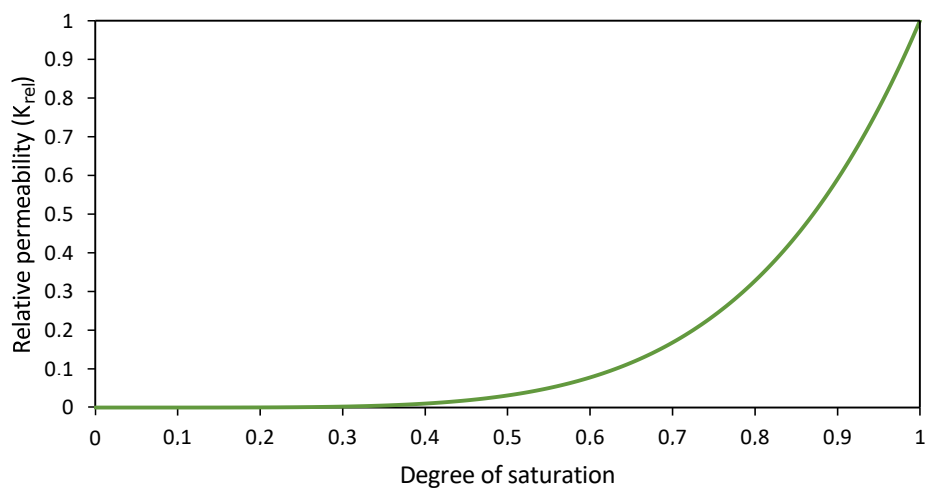


Figure 22 Degree of saturation effect on the liquid phase relative permeability

Draft

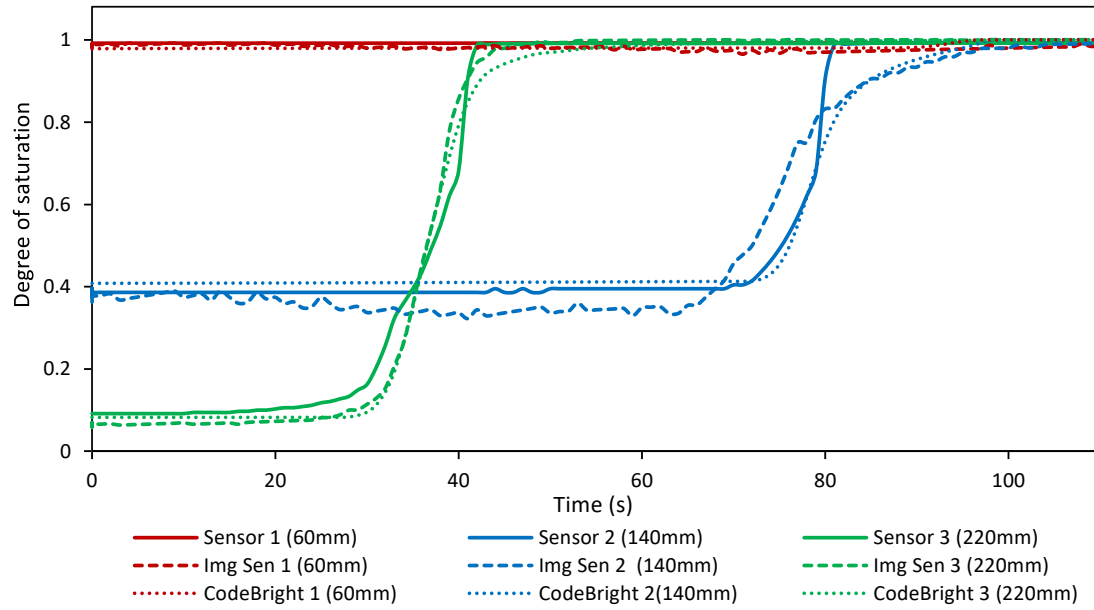


Figure 23 Comparison between the degree of saturation measured by SWIR images (dashed line), by moisture sensors (solid line) and the degree of saturation calculated through numerical simulation (dotted line) at three column heights (60 mm, 14 mm and 220 mm).

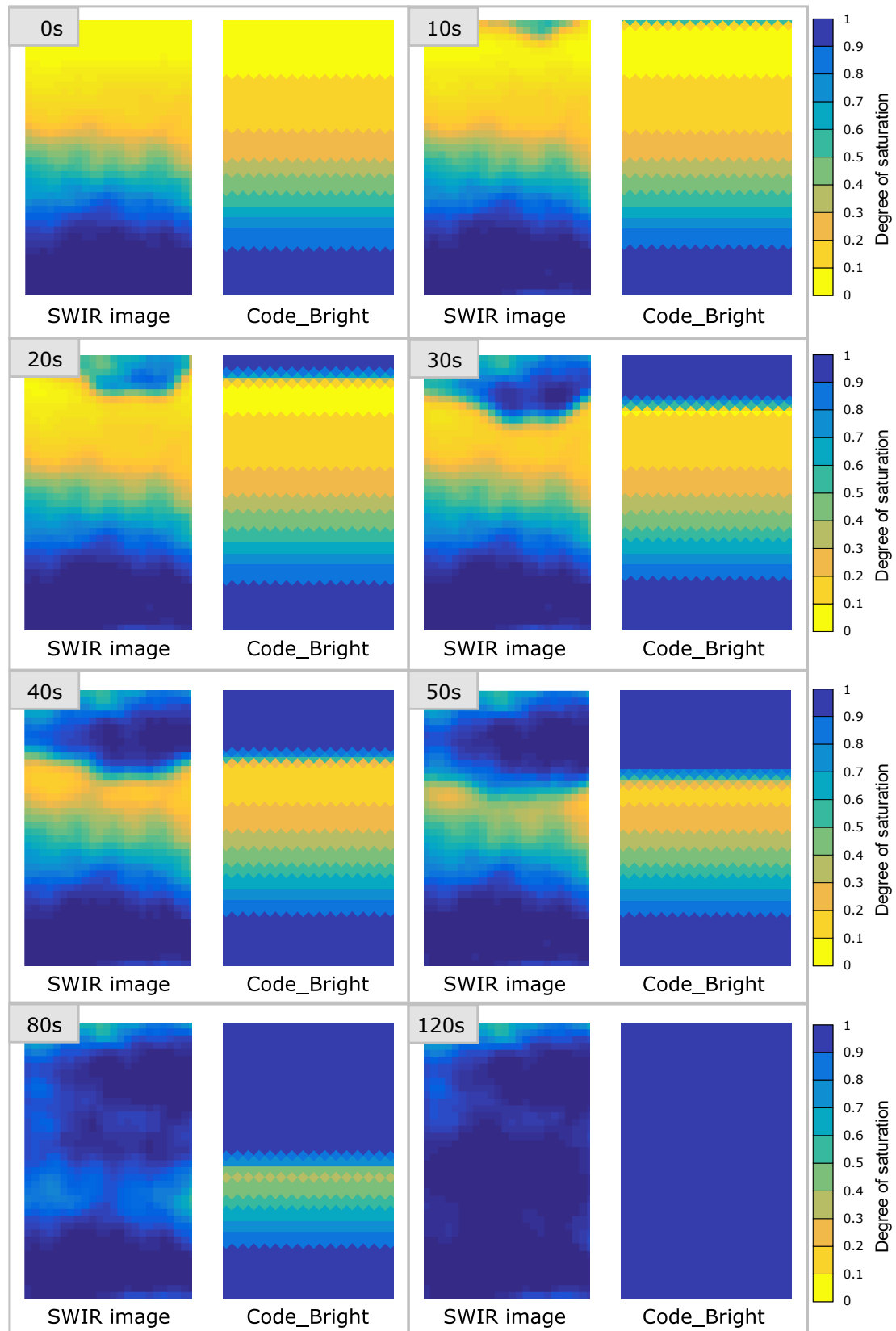


Figure 24 SWIR-measured degree of saturation compared to Code\_Bright numerical simulation at increasing time during the soil column wetting.

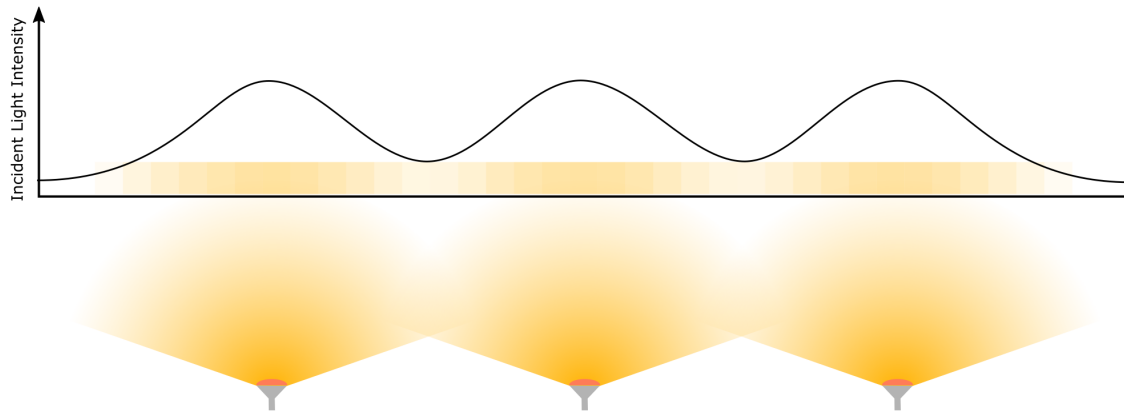


Figure 25 Example of the spatial non-uniformity of the light from 3 emitters when reaches a surface.

Draft